APPLIED SCIENCES AND ENGINEERING

Nonresonant powering of injectable nanoelectrodes enables wireless deep brain stimulation in freely moving mice

K. L. Kozielski[1,2]*[†], A. Jahanshahi[3]*, H. B. Gilbert[1,4], Y. Yu[1], Ö. Erin[1,5], D. Francisco[1], F. Alosaimi[3], Y. Temel[3‡], M. Sitti[1,6,7†‡]

Devices that electrically modulate the deep brain have enabled important breakthroughs in the management of neurological and psychiatric disorders. Such devices are typically centimeter-scale, requiring surgical implantation and wired-in powering, which increases the risk of hemorrhage, infection, and damage during daily activity. Using smaller, remotely powered materials could lead to less invasive neuromodulation. Here, we present injectable, magnetoelectric nanoelectrodes that wirelessly transmit electrical signals to the brain in response to an external magnetic field. This mechanism of modulation requires no genetic modification of neural tissue, allows animals to freely move during stimulation, and uses nonresonant carrier frequencies. Using these nanoelectrodes, we demonstrate neuronal modulation in vitro and in deep brain targets in vivo. We also show that local subthalamic modulation promotes modulation in other regions connected via basal ganglia circuitry, leading to behavioral changes in mice. Magnetoelectric materials present a versatile platform technology for less invasive, deep brain neuromodulation.

INTRODUCTION

Electrical communication with and modulation of the central nervous system (CNS) are essential to our current understanding of neurobiology and in the diagnosis and treatment of neurological disorders. Using sensing and/or modulation of neural electrical activity, key therapeutic CNS interventions have allowed remarkable medical breakthroughs. For more than 30 years, deep brain stimulation (DBS) has provided patients with symptom relief from Parkinson's disease, as well as other disorders, using electrodes wired into deep targets within the brain (*1*). More recently, closed-loop control of epidural electrical stimulation enabled walking in patients with spinal cord injury (*2*). Such devices function in freely moving patients, enabling daily activity and chronic patient use.

In recent years, efforts to make neural intervention less invasive, longer-lasting, and safer have progressed the capabilities of neural devices [For review, see (*3*)]. A key challenge of such devices is powering, and wired-in powering can require that patients undergo surgical battery changes, every 3 to 5 years in the case of DBS devices (*4*). Instead, neural devices that are remotely powered have emerged using magnetic induction (*5*), optoelectronic signaling (*6–8*), acoustic powering of piezoelectric materials (*9–14*), magnetic heating (*15*), piezoelectric powering of light-emitting diodes (LEDs) (*16*, *17*), or magnetoelectric materials (*18*), instead of a wired-in battery.

Similar to conventional DBS electrodes, centimeter-scale devices require surgery and implantation of hardware external to the CNS,

which risks brain hemorrhage, infection, and damage during daily activity (*4*). Thus, several neural device technologies have instead turned to smaller (nano- to millimeter-scale) devices, which can be completely implanted within the CNS, potentially via injection. However, smaller size can make powering of neural devices more difficult. Remotely powered devices using magnetic induction (*5*) or optoelectronic signaling (*6*, *7*) thus far are limited in their tissue penetration depth, maximally reaching 1 cm and 6 mm, respectively (*19*). Ultrasound-powered piezoelectric devices are perhaps the most promising of these technologies, recently showing recording at multiple sites through 5 cm of tissue phantom material with a sub-mm^3 device (*10*). Modulation with piezoelectric devices, however, has currently only been demonstrated in the peripheral nervous system using millimeter-scale devices or in vitro (*12–14*). As power transmission is typically done at the mechanical resonance frequency of such devices, this creates a fundamental tradeoff where an increasingly smaller device with a higher resonance frequency can be powered at increasingly shallower tissue depths (*20*, *21*). Thus, resonant coupling–based powering creates an obstacle to modulating deep brain targets with an injectable-sized device.

To circumvent signal transmission challenges, other strategies have used genetic neuronal modification and magnetothermal nanoparticles (*15*) or piezoelectrically powered LEDs (*16*, *17*) to trigger ion channel opening. However, the dependence of such technologies on transgenesis creates regulatory barriers to their translation into patients. Wireless modulation of neural activity is clinically available using transcranial magnetic stimulation (TMS), which requires no implanted device (*22*). However, TMS only modulates cortical tissue (*23*) and has a depth-focal area tradeoff (*24*, *25*), making DBS via TMS currently impossible.

To achieve wireless signal transmission to injectable devices, we have used magnetoelectric nanoelectrodes, which couple magnetic and electric signals (Fig. 1, A and B). Technologies using magnetoelectric materials for neuromodulation have previously been explored. Centimeter- and millimeter-scale magnetoelectric devices have been used for DBS, using a device mounted to the skull

[1]Department of Physical Intelligence, Max Planck Institute for Intelligent Systems, Stuttgart, Germany. [2]Department of Bioengineering and Biosystems, Institute of Functional Interfaces, Karlsruhe Institute of Technology, Karlsruhe, Germany. [3]Department of Neurosurgery, Maastricht University Medical Center, Maastricht, Netherlands. [4]Department of Mechanical and Industrial Engineering, Louisiana State University, Baton Rouge, LA 70803, USA. [5]Department of Mechanical Engineering, Carnegie Mellon University, Pittsburgh, PA 15213, USA. [6]Institute for Biomedical Engineering, ETH Zurich, Zurich, Switzerland. [7]School of Medicine and College of Engineering, Koç University, Istanbul, Turkey.
*These authors contributed equally to this work.
†Corresponding author. Email: k.koz@kit.edu (K.L.K.); sitti@is.mpg.de (M.S.)
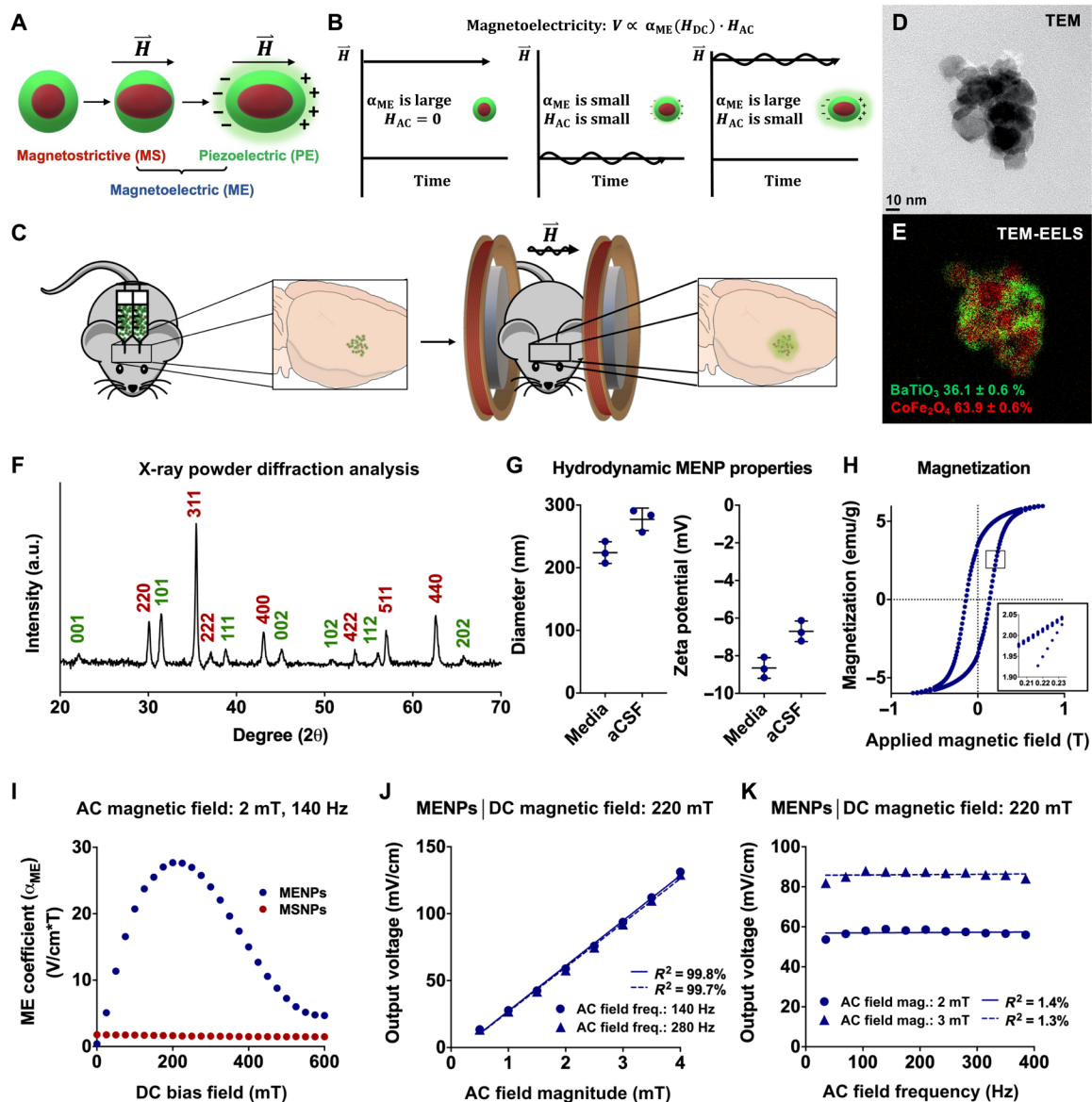‡These authors contributed equally to this work.

Fig. 1. Material and magnetoelectric characterization of MENPs made from magnetostrictive and piezoelectric phases demonstrates wireless electric field generation. Schematic demonstrating two-phase magnetoelectricity in materials made from magnetostrictive and piezoelectric materials that are strain-coupled (**A**). Schematic demonstrating the rationale for using a large DC magnetic field overlaid with an AC field to generate optimal magnetoelectric output (**B**). Diagram of method of in vivo MENP administration. MENPs are injected bilaterally into the subthalamic region of mice, and MENPs are wirelessly stimulated using an AC and DC magnetic field (**C**). Transmission electron microscope (TEM) (**D**) and TEM–electron energy loss spectroscopy (TEM-EELS) images (**E**) show MENP morphology and $BaTiO_3$/ $CoFe_2O_4$ phases (green and red, respectively), with quantitative elemental analysis measurement of the molar percentage of each material (E). MENPs were analyzed via x-ray powder diffraction (XRD) to confirm the perovskite crystal structure of $BaTiO_3$ (green) and the spinel crystal structure of $CoFe_2O_4$ (red) (**F**). a.u., arbitrary units. Dynamic light scattering (DLS) was used to characterize MENP hydrodynamic properties in cell culture media and artificial cerebrospinal fluid (aCSF) (**G**). Magnetization of MENPs was measured over a range of −1 to 1 T, as well as oscillated over a range of 0.205 to 0.235 T (inset) (**H**). emu, electromagnetic unit. The input-output magnetoelectric coefficient (α_{ME}) of particles in a sintered pellet was measured as a function of DC bias field in MENPs and MSNPs (**I**). Voltage normalized to pellet thickness of MENPs was measured using a 220-mT DC field while varying AC field magnitude (**J**). The AC field frequency dependence of α_{ME} was measured using a 220-mT DC field (**K**). Plots show individual points with means ± SD ($n = 3$) (G) and individual points fitted to a linear correlation (J and K).

and wired into the deep brain (*18*). In another study, magnetoelectric nanoparticles (MENPs) were used with the goal of achieving neuromodulation, although no replicates or statistical analysis was used to verify in vivo efficacy (*26*). Nevertheless, these studies demonstrate the promise of magnetoelectric materials for neural devices.

Here, we report wireless DBS in mice using injectable, magnetoelectric nanoelectrodes. They are implanted into the subthalamic area via stereotactic infusion, and powered using an external magnetic field at nonresonant carrier frequencies and in freely moving mice (Fig. 1C). In particular, we made two-phase MENPs using magnetostrictive $CoFe_2O_4$ nanoparticles (MSNPs) coated

with piezoelectric $BaTiO_3$. The two materials are strain coupled via sol-gel growth of $BaTiO_3$ on $CoFe_2O_4$ nanoparticles. Wireless particle stimulation is achieved by application of a magnetic field, which creates strain in $CoFe_2O_4$, resulting in applied strain to $BaTiO_3$, thereby creating a charge separation (Fig. 1A). Below, we demonstrate wireless generation of an electric field across MENPs using an applied magnetic field. We then show that magnetic stimulation of MENPs enables wireless modulation of neuronal activity in vitro and in vivo. Last, we demonstrate the therapeutic potential of this technology through its ability to modulate activity in the motor cortex and nonmotor thalamus, and to alter animal behavior.

RESULTS
Nanoelectrodes wirelessly output electric signals via the magnetoelectric effect
Two-phase MENPs were synthesized using a protocol similar to Corral-Flores *et al.* (*27*). The nanoparticles were characterized for morphology (Fig. 1, D and E), magnetostrictive to piezoelectric material ratio (Fig. 1E), and crystal structure (Fig. 1F). We observed two-phase MENPs containing $36.1 \pm 0.6\%$ $BaTiO_3$ and $63.9 \pm 0.6\%$ $CoFe_2O_4$, in their perovskite and spinel crystal structures, respectively. MENP hydrodynamic properties were also characterized via dynamic light scattering (DLS) in cell culture medium and an artificial cerebrospinal fluid (aCSF) solution. Average particle diameter was measured as 224 ± 17 nm and 277 ± 18 nm, and zeta potential was measured to be -8.6 ± 0.5 mV and -6.7 ± 0.5 mV, in medium and aCSF, respectively (Fig. 1G). Magnetization of MENPs was measured over a -1 to 1 T (Fig. 1H) and an oscillated 205 to 235 mT (Fig. 1H, inset) range.

We next measured the electrical output of MENPs under an applied magnetic field to characterize their magnetoelectric response. MENPs were measured as a sintered, poled pellet by attaching electrodes and measuring the output voltage via a lock-in amplifier (fig. S1). While this method does not allow us to take measurements of the magnetoelectric effect at the nanoscale, it can validate whether our material is magnetoelectric, and has previously been used to evaluate magnetoelectricity in core-shell particles (*28*–*30*). A pellet containing only MSNPs was used as a negative control. To optimize our ME output, we applied a small AC magnetic field with a larger DC bias field along the same axis (Fig. 1B). This orientation was used to align the magnetic domains, axis of magnetostriction, and piezoelectric poling axis to sum the magnetoelectric output along our measured axis. Application of a sinusoidal magnetic field to magnetoelectric materials outputs a sinusoidal electric field with a frequency and duration that matches the input magnetic field. Thus, we could measure this output using a lock-in amplifier (*29*). The magnetoelectric coefficient (α_{ME}), which quantifies the relationship between the input AC magnetic field and output voltage, varied nonlinearly with the DC field, as is typical of magnetoelectric materials (*31*). The α_{ME} reached a maximum of 86 V m^{-1} T^{-1} at 200 and 225 mT in the MENP pellet, while the MSNP α_{ME} showed no dependence on the DC field (Fig. 1I). Using a DC field within the maximum α_{ME} range (220 mT), we measured a linear relationship between the AC field magnitude and the voltage (normalized to pellet thickness; $R^2 = 99.8$ and 99.7% at AC frequencies of 140 and 280 Hz, respectively; Fig. 1J), which is also typical of magnetoelectric materials (*31*).

We found a low dependence ($R^2 = 1.4$ and 1.3% for AC magnitude, 2 and 3 mT, respectively) of α_{ME} on AC field frequency across the range tested (35 to 385 Hz), which covers the range of DBS frequencies found to have clinical effect (Fig. 1K) [reviewed in (*32*)]. This frequency range also has little attenuation in tissue, thus improving potential signal penetration depth (*20*, *21*).

Magnetic stimulation of magnetoelectric nanoelectrodes remotely modulates neuronal cells in vitro
The effect of wireless MENP signaling on neuronal cell activity was examined in vitro in real time using intracellular Ca^{2+} signaling in differentiated human SH-SY5Y cells. MENPs were administered at 100 µg/ml as a suspension in the imaging medium 20 min before testing, using no NPs, MSNPs, and piezoelectric nanoparticles (PENPs) as controls. Before choosing a concentration, the toxicity of MENPs was assessed with a lactate dehydrogenase (LDH) assay and a metabolic activity assay ([3-(4,5-dimethylthiazol-2-yl)-5-(3-carboxymethoxyphenyl)-2-(4-sulfophenyl)-2H-tetrazolium, MTS) (fig. S2).

Magnetic stimulation parameters were either no field, a 225-mT (within the maximum α_{ME} range) DC field, a 6-mT, 140-Hz AC field, or both DC and AC fields together using a custom coil system (fig. S3). The AC stimulation parameters were chosen to match frequencies commonly used in clinical DBS and to maximize magnetoelectric output via an increased (6 mT) AC field magnitude. The DC or AC magnetic fields alone were not expected to output a magnetoelectric effect sufficient to modulate neuronal activity and were therefore used as controls.

We found a significant increase in the percentage of cells exhibiting Ca^{2+} transients when MENPs were stimulated with a simultaneous AC and DC magnetic field ($20.1 \pm 2.3\%$) versus basal activity ($2.8 \pm 2.6\%$) (Fig. 2, A to C, and movie S1). This increase was not observed when cells were exposed to the AC and DC magnetic stimulation either alone ($1.0 \pm 1.7\%$), with MSNPs ($1.4 \pm 1.3\%$), or with PENPs ($1.4 \pm 1.2\%$), which supports our hypothesis that the measured increase in activity was due to the MENP response. While the MENPs seem to have some effect on neuronal activity ($7.2 \pm 5.0\%$, $5.2 \pm 6.0\%$, or $3.8 \pm 5.0\%$, with no field, AC field only, or DC field only, respectively), this effect was not significantly different from any other negative control group (Fig. 2, B and C, table S1, and movie S1).

To support our hypothesis that the Ca^{2+} activity we measured was related to electrophysiological cell activity, we stimulated the MENPs with AC and DC magnetic fields, but first treated the cells with either a voltage-gated Na^+ channel blocker [tetradotoxin (TTX)], a voltage-gated Ca^{2+} channel blocker (Cd^{2+}), or an extracellular Ca^{2+} chelator (EGTA) (schematic in Fig. 2D showing drug activity). In the presence of each drug, the cells failed to produce any Ca^{2+} transients (Fig. 2, D and E).

Nanoelectrodes in the mouse deep brain wirelessly modulate local brain activity
We then sought to assess the feasibility of MENP-based neuromodulation in vivo. MENPs were bilaterally injected into the subthalamic region of naïve mice (C57Bl/6J) at a dose of 100 µg per animal (1 µl total at 100 mg/ml), which was found to be tolerable in a dose toxicity assessment (fig. S4). We found no significant difference in glial fibrillary acidic protein (GFAP) or Iba-1 staining surrounding the injection site using an MENP concentration of 25, 50, or 100 mg/ml (fig. S4, C and D). We also evaluated the injection site at 48 hours, 2, and 4 weeks following injection of MENPs at 100 mg/ml and saw no qualitative signs of particle loss or changes in tissue response.
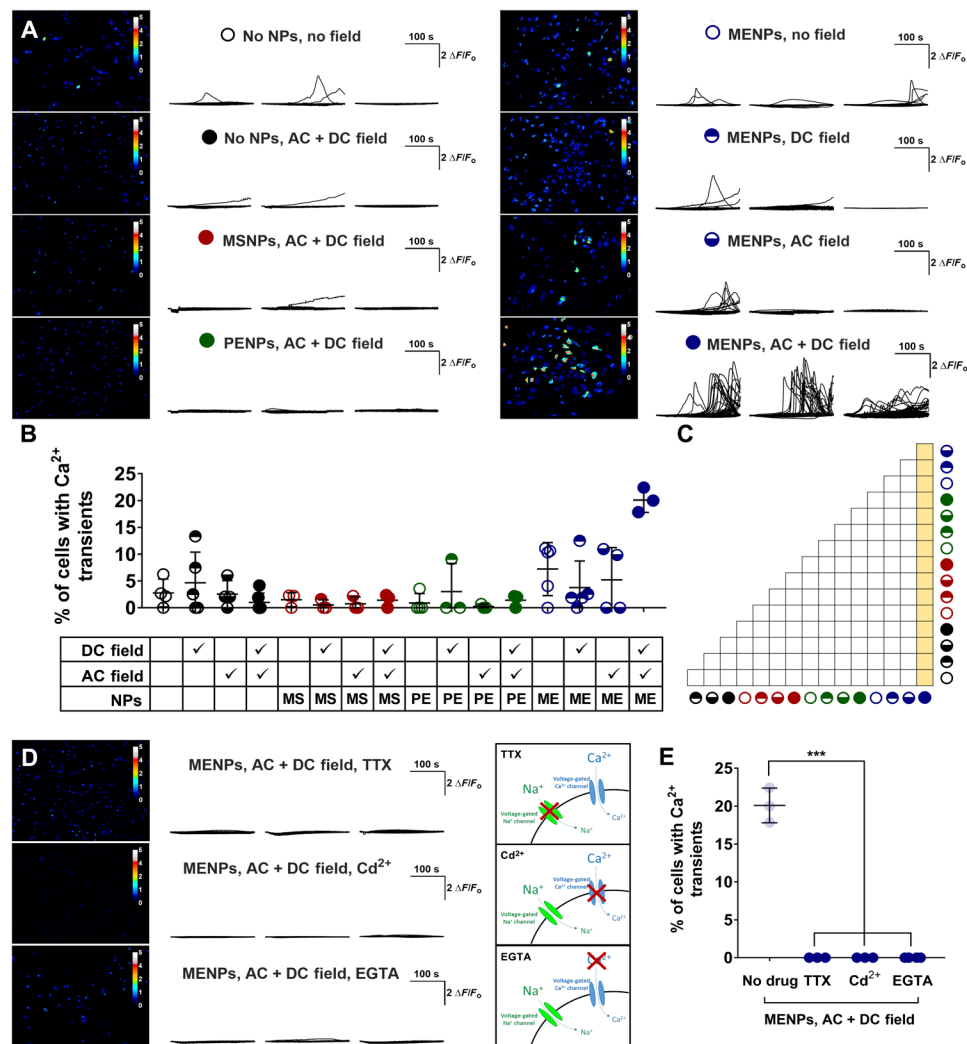
Fig. 2. Magnetic stimulation of MENPs modulates neuronal cell activity in vitro. Cells were treated with MENPs, using no NPs, MSNPs, or PENPs as controls, before magnetic stimulation. Magnetic stimulation was 220 mT DC (DC), 6 mT and 140 Hz AC (AC), or both DC and AC fields along the same axis (AC + DC). Neuronal activity was measured in real time via intracellular Ca^{2+} imaging using Fluo4 dye, and cell fluorescence was traced over time per cell. Images of total Ca^{2+} activity over time is shown for selected experimental groups. Calibration bars represent $\Delta F/F_o$ (**A**). The percent of cells demonstrating intracellular Ca^{2+} transients in (A) is summarized in (**B**), and significantly different group comparisons are marked in yellow within (**C**). Cells were treated with TTX, Cd^{2+}, or EGTA before treatment with MENPs and AC and DC magnetic stimulation, and total Ca^{2+} activity over time is shown next to a diagram depicting the inhibiting activity of each drug (**D**). Measured Ca^{2+} transients of drug-treated cells are summarized with no drug, MENP, and AC + DC field–treated cells shown as faded plot points for comparison (**E**). Plots show traces of Ca^{2+} activity over time in individual cells (A and D) and individual points with bars showing means ± SD (B and E) ($n = 3$ to 6); ANOVA with Tukey's posttest (C) or Dunnett's posttest with no drug as the control (E); ***$P < 0.001$, unlabeled group comparisons are not significantly different.

Animals euthanized at 7 weeks postinjection during phase 3 of our animal studies also showed no qualitative signs of MENP migration or loss. We analyzed the region of injection in these mice postmortem and found that the MENPs occupied a volume of 0.0088 ± 0.0023 mm³ (Fig. 3D).

During magnetic stimulation, mice were awake and unrestrained within our in vivo magnetic coil device (fig. S5). As a control group, mice were treated with MENPs and a DC magnetic field only, meaning that they were placed into the magnetic device but with the AC coil remaining off. We assessed changes in local neural activity by immunohistochemically measuring the expression of c-Fos protein, a widely used cell activity marker (33). We found significantly more c-Fos–positive cells in the region of nanoparticle injection when animals were treated with MENPs and an AC and DC field

$(38.5 \pm 8.0$ cells) versus only a DC field $(4.25 \pm 3.0$ cells) (Fig. 3, A to C). Furthermore, the volume of tissue containing c-Fos–positive tissue was significantly larger $(0.0349 \pm 0.0089$ mm³) when animals were treated with MENPs and an AC and DC field versus only a DC field $(0.0098 \pm 0.0031$ mm³). The region of tissue containing MENPs was not significantly different $(0.0090 \pm 0.0014$ and 0.0085 ± 0.0031 mm³, respectively) (Fig. 3D).

DBS via nanoelectrodes modulates basal ganglia circuitry and alters mouse behavior
We next wanted to determine whether local subthalamic neuromodulation induced by MENPs was sufficient to cause modulation in other regions of the cortico-basal ganglia-thalamocortical circuit.
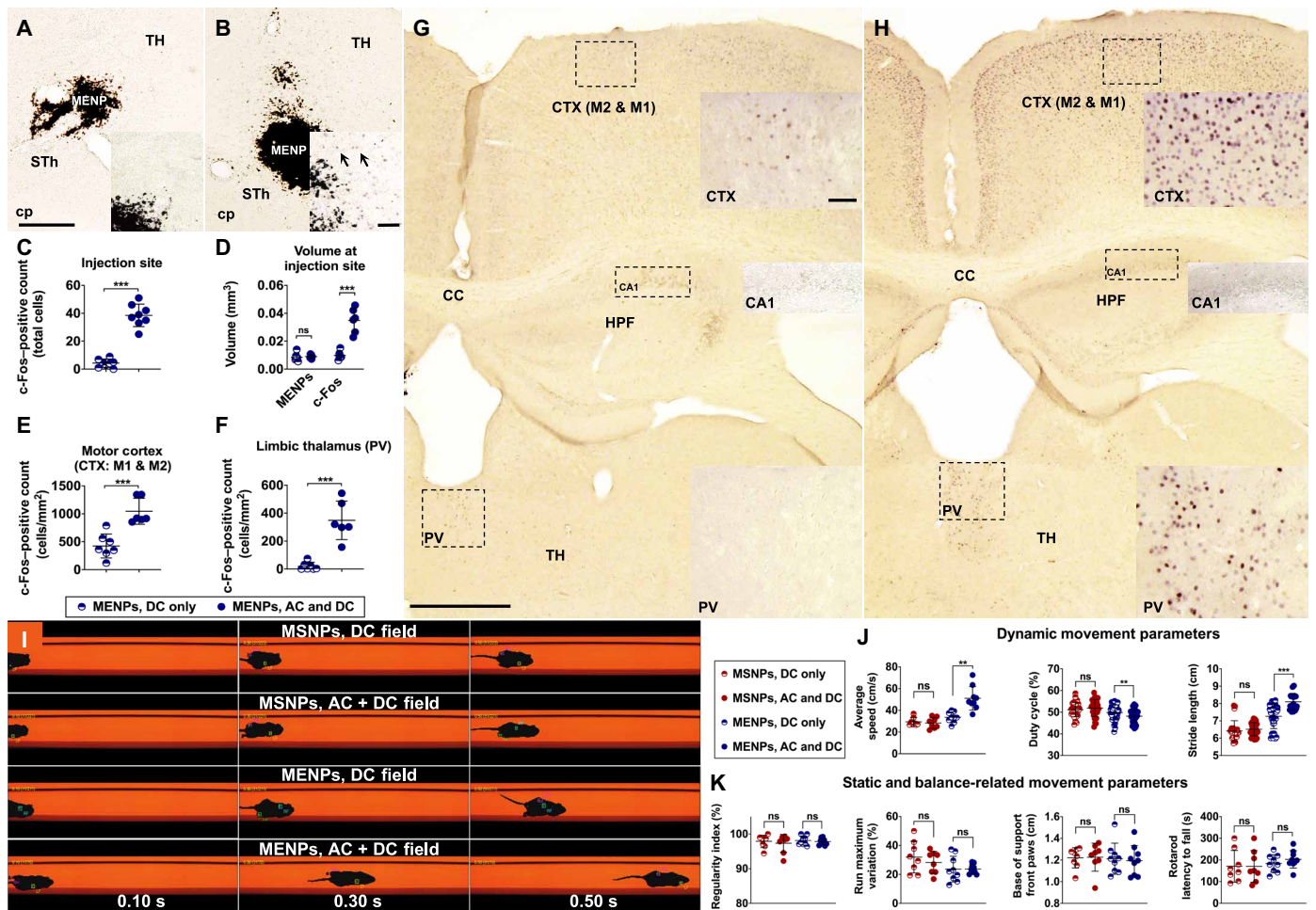
Fig. 3. Magnetic stimulation of MENPs locally modulates neural activity in mice, yielding modulation of basal ganglia circuitry and behavioral change. Staining for c-Fos protein locally to the MENP injection site following DC magnetic stimulation (**A**) or AC and DC magnetic stimulation (**B**) shows increased c-Fos expression (**C**) and increased c-Fos–positive tissue volume (**D**) in the latter. Quantification of c-Fos expression in the motor cortex (**E**) and limbic thalamus (**F**) shows increased expression when MENPs were stimulated with an AC and DC magnetic field (**H**) versus only a DC magnetic field (**G**). TH, Thalamus; cp, Cerebral Peduncle; STh, Subthalamic nucleus, HPF; Hippocampal formation; cc, corpus callosum; PV, paraventricular nucleus. Time-lapse images showing mouse movement in a CatWalk video recording system (**I**). Dynamic movement parameters as measured by the CatWalk recording showed significant changes in mouse speed, limb duty cycle, and limb stride length (**J**) in MENP-treated mice following AC and DC stimulation versus DC stimulation, while MSNP-treated mice showed no significant change. Static movement parameters of mouse movement such as regularity index, run maximum variation, and front-paw base of support as measured by CatWalk recording did not significantly change with AC and DC versus DC only magnetic stimulation in either nanoparticle group (**K**). Rotarod latency to fall also did not significantly change with AC and DC versus DC only magnetic stimulation in either nanoparticle group (K). Scale bar, 250 (overview) and 50 μm (inset) (A, B, G, and H). Plots show individual points with bars showing means ± SD (C to F, J, and K) [$n = 8$ mice (C); $n = 6$ to 7 mice (D to F); $n = 8$ to 9 mice (J and K), individual limb values for duty cycle and stride length]; unpaired t test (C to F) or paired t test (J and K), **$P < 0.01$ and ***$P < 0.001$. ns, not significant.

We found c-Fos protein expression significantly higher in the motor cortex and nonmotor thalamus following stimulation with MENPs and an AC/DC magnetic field (1046.4 ± 232.4 and 348.4 ± 137.7 cells/mm², respectively) versus only a DC magnetic field (424.8 ± 214.9 and 19.9 ± 27.6 cells/mm², respectively) (Fig. 3, E to H). We did not observe a global change in c-Fos protein expression, such as in the CA1 region of the hippocampus (Fig. 3, G and H).

To determine whether the induced neuromodulation would affect animal behavior, we tested mice via a rotarod test and the automated CatWalk XT gait analysis system. Mice were injected with MENPs or MSNPs as a control. Behavior with AC and DC magnetic stimulation versus behavior with only DC magnetic stimulation was compared for each mouse. Gait- and balance-related static parameters during the CatWalk test, such as regularity index, run

maximum variation, and base of support, showed no significant difference following AC and DC stimulation in either nanoparticle group (MSNPs: 97.3 ± 2.5 versus 97.9 ± 1.8%, 28.3 ± 7.6 versus 31.9 ± 11.0%, and 1.2 ± 0.1 versus 1.2 ± 0.1 cm, DC versus AC and DC stimulation, respectively) (MENPs: 97.8 ± 1.0 versus 98.1 ± 1.3%, 23.7 ± 3.3 versus 23.6 ± 8.9%, and 1.2 ± 0.1 versus 1.2 ± 0.1 cm, DC versus AC and DC stimulation, respectively) (Fig. 3, J and K, and movie S2). Rotarod testing also showed no significant difference in latency to fall with either nanoparticle group (MSNPs: 170.4 ± 72.9 versus 170.9 ± 73.2 s; MENPs: 202.6 ± 40.4 versus 184.0 ± 40.5 s, DC versus AC and DC stimulation) (Fig. 3K). Overall, no significant difference in measured gait and balance parameters was found between the groups. This was important to establish that magnetic stimulation of MENPs caused no determent to animal motor activity.

Conversely, in analyzing the speed-related and dynamic parameters of the CatWalk test, which are indicative of high-speed gait, we found a significant difference in the behavior of MENP-treated animals that was not observed in MSNP-treated animals (Fig. 3, J and K, and movie S2). The average speed, duty cycle of each limb, and stride length of each limb all changed significantly in MENP-treated mice following AC and DC stimulation (51.1 ± 10.9 versus 33.6 ± 4.8 cm/s, 48.1 ± 3.0 versus 49.9 ± 3.5%, and 8.1 ± 0.5 versus 7.3 ± 0.7 cm, DC versus AC and DC stimulation, respectively) but not in MSNP-treated mice (28.3 ± 5.0 versus 29.4 ± 3.8 cm/s, 51.9 ± 3.9 versus 51.1 ± 3.2%, and 6.5 ± 0.4 versus 6.4 ± 0.6 cm, DC versus AC and DC stimulation, respectively).

DISCUSSION

As the potential applications of neural devices have increased, new technologies to make neural intervention safer, longer-lasting, and less invasive have generated interest in smaller and wireless devices. Remote powering of neural devices not only allows for smaller device sizes but can also eliminate the need for bulky equipment or surgical battery changes. Recently, several remotely powered devices have emerged that could enable less invasive neuromodulation, with some even reaching deep brain sites (3, 12–18). The most clinically promising of these do not rely on transgenesis of neural tissue but instead directly create electric signals to achieve neuromodulation (12–14, 17, 18). However, it has not yet been possible to scale down such devices sufficiently to enable complete implantation in the brain while still achieving deep brain neuromodulation.

In this work, we used MENPs as nanoelectrodes, with the goal of wirelessly modulating neuronal activity using remote powering via a magnetic field. We characterized the magnetization of the MENPs, particularly looking at a field range oscillated over the range of fields used during in vitro and in vivo experiments, and found no magnetic hysteresis (Fig. 1H, inset). This is important to show that the MENPs would not produce heat during in vitro and in vivo experiments, thus eliminating heat as a source of off-target neuromodulation.

We characterized the magnetoelectric response of the nanoelectrodes as a sintered pellet, particularly looking at electrical output as input magnetic field changed. While a magnetoelectric response can be initiated with just an AC magnetic field, large AC fields are required to approach the maximum α_{ME}, which would require powerful coil systems and additional components to enable active cooling. Instead, we applied a large DC magnetic field using permanent magnets and overlaid a smaller AC field to maximize α_{ME} (Fig. 1, B and C, and figs. S3 and S5). While varying each input component (i.e., DC field magnitude, AC field magnitude, and AC field frequency), we determined that the MENP nanoelectrodes output an electric response characteristic of magnetoelectric materials (Fig. 1, I and J). We did not find this behavior using magnetic only, MSNPs.

An important finding in this study that corresponds with previous work in magnetoelectric materials is that the magnetoelectric output had a low dependence on the input, carrier AC field frequency (Fig. 1K). While α_{ME} increases sharply near the mechanical resonance frequency of magnetoelectric materials, α_{ME} otherwise remains relatively constant (34). In this study, our carrier magnetic signals were far from the resonant frequency range of nanoscale materials (140 Hz versus GHz range). Previous neural device technologies based on piezoelectric and magnetoelectric materials have

often relied on carrier frequencies that provide resonant coupling for remote powering (12, 13, 18). However, this fundamentally creates an inverse correlation between device sizes as compared to carrier frequency and possible tissue penetration depth. As a result, such devices have been unable to demonstrate neuronal modulation in deep brain tissue using injectable-sized devices.

As resonant coupling–independent signaling to magnetoelectric materials yields a lower α_{ME}, we next needed to determine whether signaling to MENPs away from resonance would yield sufficient output electric signaling to modulate neuronal activity. Resonant coupling to magnetoelectric materials has been shown to generate electric fields much higher than the necessary threshold for neuromodulation (18). We therefore hypothesized that using magnetoelectric materials and resonant coupling–independent signaling, we would be able to modulate brain activity using nanoscale materials.

We first assessed this in neuronal cells in vitro, measuring intracellular Ca^{2+} as a second messenger of electrophysiological activity. As we showed earlier that both the large DC and small AC magnetic fields were necessary to generate a magnetoelectric output (Fig. 1, I and J), we used the AC and DC fields individually as controls for potential side effects caused by the magnetic fields alone. We also used PENPs and MSNPs as material controls, as neither piezoelectric nor magnetostrictive materials alone generate an electric output to a magnetic input, so any cell activity increases with these materials would signal modulation due to extraneous effects. Cells in all control combinations tested showed no significant difference in the percent of cells displaying Ca^{2+} transients, while AC and DC magnetic stimulation of MENPs significantly increased cells with transients versus all other controls (Fig. 2, A to C).

To support our hypothesis that the measured Ca^{2+} transients were due to the electrophysiological activity of the cells, we treated cells with drugs to independently block the activity of voltage-gated Na^+ channels, voltage-gated Ca^{2+} channels, or extracellular Ca^{2+} sources. With the application of these drugs, magnetic stimulation of MENPs showed significantly lower neuronal Ca^{2+} activity versus stimulation without blocking drugs (Fig. 2, D and E). This substantiates the dependence of our measured Ca^{2+} transients on voltage-gated ion channels and extracellular Ca^{2+} sources, supporting the relationship between our measured Ca^{2+} activity and cell electrophysiological activity.

Next, an in vivo study was conducted to assess the feasibility of MENP-based DBS. To this aim, naïve mice received bilateral injection of MENPs in their subthalamic region. The injected MENPs were stimulated using an AC and DC magnetic field, with a DC field only serving as a control. The rationale behind region selection was that the basal ganglia and the subthalamic region are common target areas for DBS (35). Moreover, these areas have been thoroughly studied with regard to brain circuits in the field of DBS and neuromodulation for neurological disorders (36, 37). These structures are connected to higher (cortical via thalamus) and lower (brainstem) areas through both partially parallel and partly integrated projections. These projections are primarily responsible for motor control, as well as other functions such as motor learning, associative functions, and emotions. According to the classical basal ganglia model, information flows through the basal ganglia back to the cortex through two pathways, while new models show that parallel circuits subserve the classical functions of the basal ganglia, engaging associative and limbic territories (38, 39). Therefore, the cortico-basal ganglia-thalamocortical circuit provides a useful tool

to reliably investigate the effects of neuromodulation on a wide range of behavioral functions.

MENPs were implanted using stereotactic injection into the subthalamic region. Using a dose of 100 μg per animal, we determined that the MENPs occupied a volume comparable to a conventional rodent DBS electrode (0.3 mm in diameter). As both a conventional DBS electrode and the MENPs could displace tissue upon implantation, this coverage area could control for a potential sham effect. A dose toxicity assessment of tissue following MENP injection at different concentrations led us to confirm this concentration, as it showed no significant change in inflammatory markers versus other concentrations tested (fig. S4, C and D). A qualitative evaluation of this particle dosage showed no change in the volume of MENPs or the tissue response to the MENPs over a 4-week period. The injected MENPs were also still present at the site of injection 7 weeks postinjection (Fig. 3A).

We evaluated local neuronal activity in the region of MENP injection using an antibody against c-Fos, a widely used cell activity marker (33). Quantification of stained sections showed a significantly higher number of c-Fos–positive cells in the region of MENP injection in animals treated with AC and DC fields versus only a DC field (Fig. 3, A to C). We also found a significantly larger volume of tissue containing c-Fos–positive cells surrounding MENPs stimulated with an AC and DC magnetic field versus only a DC field (Fig. 3D). These data support our hypothesis that we could wirelessly modulate local brain activity using the magnetoelectric response of MENPs to magnetic stimulation.

To determine whether the local neuronal activity induced by MENPs was sufficient to drive neuronal activity in thalamocortical pathways, we assessed c-Fos protein expression in other regions of the brain. We found that c-Fos protein expression is significantly higher in the motor cortex and paraventricular nucleus (PV) of the thalamus following stimulation with MENPs and an AC/DC magnetic field versus only a DC magnetic field (Fig. 3, E to H). We observed a selective, not global, c-Fos protein expression in the brain of stimulated animals. Together, these data support our hypothesis that the measured increases in c-Fos protein expression were due to local subthalamic stimulation of the cortico-basal ganglia-thalamocortical circuit and not a nonspecific, global modulation of neural activity via the magnetic field.

Next, we tested the mice in a rotarod test and the automated CatWalk gait analysis system to determine whether the induced neuronal modulation in thalamocortical pathways would affect animal locomotion. Gait- and balance-related static parameters during the CatWalk test, which measure motor function, showed no significant difference following AC and DC stimulation in either nanoparticle group (Fig. 3, I to K). Rotarod testing also showed no significant difference in latency to fall with either nanoparticle group (Fig. 3K). While we anticipated no improvement in motor function, as we tested only naïve mice, these results are important to demonstrate that we saw no detrimental effect to the gait and balance of the animals due to neuromodulation via MENPs. This finding of no generalized behavioral change also corresponds to our c-Fos expression findings, in which we found only selective expression changes.

When analyzing the dynamic parameters of the CatWalk test, which are indicative of animal speed, we found a significant change in the behavioral parameters of MENP-treated animals, but not MSNP-treated animals (Fig. 3, I to K). Specifically, we saw an increase in speed, which concomitantly lead to an increase in stride length, and a decrease in duty cycle (i.e., a decrease in the percentage of each stride spent in stance versus swing). The aforementioned selective behavioral responses are intriguingly in line with selective c-Fos expression in the PV. Current literature presents ample evidence that the PV relays information projected from the brainstem and subthalamic areas to the nucleus accumbens and the amygdala, as well as the cortical areas associated with these subcortical regions (40). Selective activation of the PV is known to produce states of arousal that contribute to fear, anxiety, reward regulation, and defensive behavior (40). Expression of different gaits is adapted to behavioral demands during locomotion. In this regard, alternating gaits like walking and exploration take place at slower locomotor speeds, while synchronous gaits during escape are present at fast locomotor speeds (41). Although the exact neuronal substrate(s) behind them have not yet been elucidated, recent evidence suggests that low- and high-speed gaits arise from distinct midbrain areas (42). Given that the static versus dynamic CatWalk gait parameters are more likely to be affected during low- versus high-speed locomotion, respectively, it is conceivable that dynamic gait parameters are mainly altered because of increased running speed in this study.

On the basis of this evidence, we believe that the measured changes in animal speed are due to wireless subthalamic stimulation via MENPs. The combined results of c-Fos protein immunohistochemistry and animal behavioral tests support the conclusion that magnetically stimulated MENPs wirelessly modulated neurons within deep brain sites to affect brain behavior. On the basis of these data, we suggest that the MENPs were able to evoke specific behavioral changes correlated with selective perturbation in the thalamocortical circuit.

While we found changes in animal behavior linked to anxiety, in the future, it will be important to assess the therapeutic effect of wireless modulation in animal disease models. Healthy animals would not be expected to show a benefit in motor function with successful DBS. Therefore, in this study, we could only assess animal locomotion to determine that we did not detrimentally affect movement. Studying DBS via magnetoelectric nanoelectrodes in a Parkinsonian model will, in the future, be necessary to measure a benefit to motor function.

A key finding of this work is that resonant coupling–independent remote powering of a neural device yields sufficient electrical activity to modulate brain activity. This decouples the relationship between device size and potential powering depth, enabling nanoscale materials to modulate deep brain tissue. Modeling of carrier signal transmission through tissue to magnetoelectric devices would benefit future device design and elucidate limitations on tissue penetration to human-scale deep brain targets. Furthermore, future work will be necessary to understand how the carrier frequency is propagated by the MENPs into a stimulating signal that is received by neurons, as temporal control of stimulation is the key to the therapeutic effects of DBS (43, 44). The exact mechanism of neuronal modulation also remains an open question. Hence, future work will be necessary to learn more about the various input parameters (e.g., nanoparticle concentration, magnetic stimulation magnitude, stimulation frequency, and duration) that enable modulation. As the electric field gradient along an axon has been shown to be a key determinant in activation (45, 46), we hypothesize that the mechanism of action may be related to high gradients generated along the very small nanoparticles. However, field gradients at the nanoscale have never been evaluated in relation to neuronal activation. We would require a better understanding of the magnetoelectric

response at the nanoscale, as well as how the MENPs and their fields interact, to speculate further. With regard to the longevity of the MENPs, while we know that they remain at the injection site and modulate neurons as long as 7 weeks postinjection, translation of this technology to patients would require a further study of the long-term compatibility, immune response, and functionality of the nanoparticles. However, this work represents an important proof of concept in remote powering of nanoscale neural devices.

The results herein demonstrate the potential of magnetoelectric materials as nanoelectrodes for wireless electrical modulation of deep brain targets. We have shown that we can stimulate MENPs with a magnetic field to remotely generate electric polarization of the MENPs. We have shown evidence that nonresonant magnetic powering of MENPs locally modulates neuronal activity in vitro and in vivo. We have also demonstrated that this modulation is sufficient to change animal behavior and to modulate other regions of the corticobasal ganglia-thalamocortical circuit. Future work will be the key to optimizing magnetoelectricity-based neural devices and understanding the abilities and limitations of this technology. Magnetoelectric nanoelectrodes show promise for new technologies in wireless neural devices.

MATERIALS AND METHODS
Study design
The objective of this study was to assess the potential of MENPs to wirelessly modulate neuronal activity via a magnetoelectric response to an applied magnetic field. This was approached by applying a magnetic field to the MENPs (and control nanoparticles) and measuring (i) their output electric signaling, (ii) their ability to modulate neuronal cell activity in culture, (iii) their ability to modulate brain activity in mice, and (iv) the effect of this modulation on mouse behavior. While an ongoing and measurable magnetoelectric effect was expected only when applying a large DC magnetic field overlaid with a smaller AC magnetic field, AC and DC magnetic field application alone were used as experimental controls. All experiments in this study were carried out via controlled laboratory experiments. Sample sizes were determined independently for each experiment without formal power analysis. Where appropriate, references used to determine sample size are cited. Sample size is listed in the methods of each experiment, as well as in the figure captions where results are shown. The methods below also include a description of how sample size corresponds to sampling versus experimental replicates. Endpoints varied by experiment and are listed below. Exclusion criteria for animal safety are listed below in the description of the toxicity analysis. However, no animals were excluded from the study due to these criteria. Animal behavioral testing was done with the experimenter and data analyst blind to animal identity. Information regarding cell line, animals, and antibodies used is listed below. Ethical oversight and approval of animal studies are listed below.

MENP synthesis
MENPs were synthesized in a manner similar to Corral-Flores et al. (27). $CoFe_2O_4$ nanoparticles (30 nm; Sigma-Aldrich) were suspended in deionized water (dH_2O) at a concentration of 10 mg/ml to 80°C while stirring. Oleic acid was added to the suspension at 30 weight % with respect to $CoFe_2O_4$, the temperature was raised to 90°C for 30 min and then lowered to 60°C. Octane was added to the suspension at a 1:1 ratio to the dH_2O volume, which separated oleic acid–coated

$CoFe_2O_4$ particles into the organic layer. The organic layer was then washed with dH_2O three times. Barium acetate and titanium butoxide were dissolved in glacial acetic acid with stearic acid (final concentration, 0.01%) such that the final molar ratio of $BaTiO_3$ to $CoFe_2O_4$ was 1:3. This solution was stirred and heated to 90°C, the $CoFe_2O_4$ solution was added, as well as 2-methoxyethanol, at a final volume concentration of 30%. The solution was dried, calcined at 700°C for 2 hours, and then ground with a mortar and pestle. MSNP control particles were the unmodified, commercially available $CoFe_2O_4$ nanoparticles used as the MENP core. PENP control particles were commercially available $BaTiO_3$ nanoparticles (50 nm; Sigma-Aldrich). To select for particles with better colloidal stability, all nanoparticles were suspended in dH_2O and centrifuged for 1 min at 10g, and particles within the supernatant were kept for further experiments.

X-ray diffraction analysis of MENP crystal structure
X-ray diffraction (XRD) analysis of MENPs was carried out on a Bruker D8 Advance Powder Diffractometer using Cu radiation generated at 40 kV/40 mA with a Bragg-Brentano beam path. A divergence slit at 0.5°, antiscatter slits at 2° and 4°, and Soller slits were used. The output beams were received using a VÅNTEC-1 one-dimensional (1D) detector. Peaks were identified using the International Centre for Diffraction Data database. MathWorks MATLAB software was used to baseline-correct the spectrum, using the *msbackadj* function.

Elemental analysis of MENPs to determine chemical composition
MENP elemental analysis was carried out via inductively coupled plasma (ICP)–optical emission spectrometry using a Spectro Ciros spectrometer (Kleve, Germany). MENPs were first dissolved in an aqueous solution of 3% HNO_3 and 1% HF before sample loading in the spectrometer. Data were analyzed using Spectro ICP Analyzer software to detect Ba, Ti, Co, and Fe spectra. Data are presented as the means ± SD of each element measured within $BaTiO_3$ and $CoFe_2O_4$.

Transmission electron microscopy and electron energy loss spectroscopy analysis of MENP morphology
MENPs were prepared for transmission electron microscopy (TEM) analysis by drop-casting an aqueous suspension onto C-coated Cu TEM grids and air-drying. TEM and TEM–electron energy loss spectroscopy (EELS) images were acquired using a Zeiss Sub-Electron-volt Sub-Angstrom Microscope. Data were acquired in TEM mode at 200 kV. For EELS, we acquired energy-filtered TEM spectrum images from 30 to 120 eV, with 3-eV steps and 4× binning. After data acquisition, the EELS signal from Ba ($N_{4,5}$ edge, 90 eV) and Fe ($M_{2,3}$ edge, 54 eV) was extracted and used for the elemental map.

Analysis of MENP hydrodynamic properties
Hydrodynamic diameter and zeta potential of MENPs were measured via DLS using a Wyatt Mobius DLS Instrument and analyzed via Wyatt DYNAMICS software. MENPs were diluted to a concentration of 100 μg/ml in either our cell culture differentiation media (see below) or an aCSF solution (47) during the measurements. Data were analyzed from three independent experiments.

Analysis of MENP magnetic properties
A Microsense EZ vibrating sample magnetometer (VSM) was used to measure the magnetic properties of MENPs. MENPs were measured using 6 mg of MENPs as a powder, held to the VSM probe using

wax. Magnetization was measured over a range of −1 to 1 T, as well as oscillated over a range of 205 to 235 mT.

Formation of sintered pellets of nanoparticles and pellet wiring

For ME measurement of pellets, 0.65 g of MENPs were mechanically pressed into a pellet of diameter of 8 mm using 6 tonnes/cm^2 of pressure and then sintered at 1150°C for 12 hours. MSNP pellets were prepared in the same way but using only $CoFe_2O_4$ nanoparticles. The circular surfaces of the pellets were painted with conductive silver glue to attach copper plates (fig. S1A). Pellets were heated to 140°C, electrically poled at thickness of 1 kV/mm for 5 min, and then allowed to cool to room temperature while maintaining the applied voltage. The pellets were then wired to a charge amplifier. The pellet and charge amplifier were enclosed in a Faraday shield and connected externally to a lock-in amplifier for voltage measurement (fig. S1, B to H).

Charge amplifier design

For electrical measurement of the magnetoelectric response of pellets, a charge amplifier is used to eliminate the effects of stray capacitance on the measurement of the piezoelectric charge. The battery-powered amplifier was constructed on a standard FR4 printed circuit board, which was placed within the Faraday shield. The charge amplifier uses an operational amplifier circuit (fig. S1, F to H) based on the Texas Instruments OPA340. The amplifier has a high-pass characteristic with a −3 − dB frequency of 3 Hz, and the calculated gain of the circuit in the passband is 200 mV/pC.

Magnetoelectricity measurements

A Microsense EZ VSM was used as a DC magnetic field source and was modified to hold an additional, smaller Helmholtz coil. This was powered with a signal generator (35- to 385-Hz sine wave) connected to a linear voltage amplifier (Hewlett Packard) to provide current to the smaller coils, generating an AC magnetic field in the plane of the sample. The pellet was oriented such that the AC and DC magnetic fields were parallel to the pellet's central axis (fig. S1E). The AC magnetic field magnitude was measured using a gaussmeter before experimentation. Pellets were demagnetized before all measurements.

Culture and differentiation of SH-SY5Y neuronal cells

SH-SY5Y cells were purchased from the Deutsche Sammlung von Mikroorganismen und Zellkulturen (DSMZ) (American Type Culture Collection CRL-2266). Maintenance cultures were grown in Dulbecco's modified Eagle's medium (DMEM)/F12 (Gibco) with 10% fetal bovine serum (FBS) and 1% penicillin/streptomycin, at 37°C with 5.0% CO_2. Media was changed every 3 to 4 days. Before plating for experiments, wells were coated with laminin (5 μg/ml) in phosphate-buffered saline (PBS) with Ca^{2+}/Mg^{2+} for 1 hour at 37°C. For Ca^{2+} signaling experiments, cells were plated at a concentration of 20,000/cm^2 onto cell culture–treated, four-well IBIDI μ-slides. For toxicity analysis, cells were plated at a concentration of 20,000/cm^2 onto cell culture–treated 96-well plates. Experimental cultures were differentiated in DMEM/F12 medium containing 1% FBS, 1% penicillin/streptomycin, and 10 μM retinoic acid (Sigma-Aldrich) for 4 days before all experiments.

Analysis of cell toxicity

MENPs were suspended in experimental cell culture medium at a concentration of 0, 50, 100, 200, or 300 μg/ml and added to cells.

Toxicity was assessed at 24 hours following MENP administration via a CyQUANT LDH assay kit (Thermo Fisher Scientific), as well as a CellTiter 96 AQueous One MTS assay. Assay results were read using a BioTek Synergy 2 Microplate Reader (fig. S2). Each experiment was tested within four wells, and the average of these values was recorded to provide a single data point. The data were analyzed from three independent experiments.

In vitro magnetic stimulation

A magnetic stimulation setup was designed to fit into a Zeiss Axio Observer A1 microscope and to hold a four-well IBIDI μ-slide (fig. S3). A DC magnetic field was provided by three permanent NdFeB magnets (N42, 6 cm in diameter, 5 mm in height; Supermagnete) on either side of the cells to generate a 225-mT field at the center of the cell culture well. A magnetic coil was used to provide an AC magnetic field along the same axis. AC signals were generated by a National Instruments DAQ USB X-Series device, controlled via LabVIEW software, and amplified by a class D audio amplifier. For all experiments with AC magnetic stimulation, the AC field component was a 6-mT sine wave at 140 Hz applied during the time window of 10 to 30 s during the time-lapse recording. AC and DC magnetic field magnitudes were verified with a magnetometer.

Ca^{2+} signaling experiments

Cells were loaded with 1 μM Fluo4-AM dye (Thermo Fisher Scientific) in Live Cell Imaging Solution (LCIS; Invitrogen) for 30 min at 37°C. Experimental suspensions of no NPs, MENPs, PENPs, or MSNPs were prepared at 100 μg/ml in LCIS. After Fluo4 loading, cells were washed three times with LCIS, and particle suspension solutions were added. Cells with particles were incubated for 20 min at 37°C to allow Fluo4 to deesterify and then moved onto a Zeiss Axio Observer A1 microscope mounted with the in vitro coil system. For experiments using inhibitory drugs, Fluo4 loading was carried out as described above, and drugs were added in the LCIS with MENPs after washing. For EGTA, PBS was used instead of LCIS and was added during the Fluo4 loading step. TTX was added at a concentration of 100 nM, $CdCl_2$ (Cd^{2+}) was added at 100 μM, and EGTA at 5 mM, which have previously been determined to be inhibitory but nontoxic concentrations (14).

Fluo4 was excited using a 470-nm LED with a 484/25-nm excitation filter and observed through a 519/30-nm emission filter. Time-lapse images were taken at ×10 magnification, every 1 s for 240 s using 50-ms illumination and recorded using a Zeiss Axiocam 503 mono camera (2.8 megapixels). Data were collected from three to six independent experiments per group.

Time-lapse recordings were analyzed using ImageJ software. Briefly, the first 10 images of each time lapse were stacked into a single image to enable region of interest (ROI) selection. Following brightness normalization, blurring, background subtraction, and thresholding, ROIs were selected from this image using the Analyze Particles function (with all settings remaining consistent for all time lapses). These ROIs were then overlaid onto the completely unmodified time-lapse series, and the mean gray value within each ROI was recorded for each frame. These values were then used to calculate Ca^{2+} transient amplitudes as $\Delta F/F_o$. Cells positively showing Ca^{2+} transients were calculated using MathWorks MATLAB software, using a linear baseline correction and the *peakfinder* function. Images in Fig. 2 (A and D) were generated by creating a maximum value Z-stack of the entire video.

Animals

Experiments were performed on 65 male naïve mice (C57Bl/6J; the Jackson Laboratory). Mice were socially housed under controlled conditions (21° ± 2°C and 40 to 60% humidity) in a reversed 12-hour day/night cycle (lights on, 7 p.m.) until they had received surgery. Mice were given ad libitum access to food and water. At the time of surgery, mice were 3 months of age. Experiments were conducted according to the directive 2010/63/EU for animal experiments and in agreement with the Animal Experiments and Ethics Committee of the Maastricht University, Maastricht, The Netherlands.

Stereotactic nanoparticle administration

Buprenorphine (0.1 mg/kg) was subcutaneously injected half an hour before surgery as an analgesic. Inhalational anesthesia was induced and maintained with isoflurane (Abbot Laboratories, Maidenhead, UK) at 4% and 1.5 to 3%, respectively. After adequate induction of the anesthesia, the mouse was placed in a small animal stereotaxic frame (Stoelting, Dublin, Ireland) and fixed by ear bars with zygoma ear cups (Kopf, Los Angeles, USA) and a mouse gas anesthesia head holder (Stoelting, Dublin, Ireland). To maintain body temperature at 37°C throughout the whole procedure, the mouse was placed on a thermoregulator pad. An ocular lubricant was applied to prevent drying of the eyes. A subcutaneous injection of 1% Lidocaine (Streuli Pharma, Uznach, Switzerland) at the incision side was given for local anesthesia.

Consecutively, burr holes above the subthalamic area [anterior-posterior (AP): −2.06 mm, medial-lateral (ML): ±1.50 mm, dorsal-ventral (DV): −4.50] were made, and a total of 2 μl of MENPs or MSNPs was injected with a microinjection apparatus Nanoject II (Drummond Scientific). The infusion rate was 100 nl/min. After the injections, the syringe needle remained inside the brain for another 10 min before a slow withdrawal.

In vivo magnetic stimulation

All in vivo magnetic stimulation was carried out using a custom coil system that would allow mice to move freely during the experiments. The animal experiment setup was designed to provide a 220-mT DC magnetic field with a 6 mT, 140-Hz AC magnetic field along the same axis at the center of the animal chamber. Images and the design of the in vivo coil system are shown in fig. S5. The structure was 3D-printed with Acrylonitrile Butadiene Styrene using a uPrint SE Plus 3D printer. A DC magnetic field was provided by six NdFeB disk magnets (N42, 6 cm in diameter, 5 mm in height; Supermagnete) on each side of the animal chamber. As safety precautions, the permanent magnets were covered with a protective lid, and the animal holder base was 3D-printed using the solid option for higher durability. The AC magnetic field was provided by two coils on either side of the animal chamber. A 1-mm-thick copper wire was wound around a 3D-printed plastic coil frame with 360 turns each. Corresponding coil-pair resistance was 4.94 ohm, and coil-pair inductance was 24.5 mH. A Voltcraft 8210 signal generator was used to provide a 140-Hz sine wave, which was amplified using a QSC-GX7 power amplifier. These were then connected to the AC coils. AC and DC magnetic field magnitudes were verified with a magnetometer. For all AC and DC stimulation experiments, mice were stimulated with the coil turned on for 180 s. For DC only stimulation experiments, mice were placed into the animal chamber for 180 s with the coil remaining off.

Description and timelines of animal experimental procedures
Phase I: Toxicity assessment

We first adjusted optimal concentration of MENPs. Three doses were tested, including 25, 50, and 100 mg/ml. Mice were randomly assigned to either 25, 50, or 100 mg/ml test groups ($n = 8$) and received stereotactic injection of MENPs (fig. S4A). Animals were monitored for signs of sub- or epidural hemorrhage, neurological symptoms of the injection, welfare (weight, responsiveness, and water intake), and discomfort/pain. No animals were eliminated from the experiments due to failing these criteria. Fourteen days after the surgery, mice were euthanized for immunohistochemical (IHC) analysis of the brain as described below. Five brains were randomly selected for IHC. Sections belonging to one mouse were excluded as tissue ruptured during processing. Brain sections were processed using antibodies raised against astrocytes and microglia (fig. S4, B and C). Another series of brain sections were stained using standard hematoxylin and eosin (H&E) to evaluate tissue damage at the site of injection (fig. S4D).

Phase II: Persistence of nanoparticles at injection site and c-Fos protein expression

Mice were randomly assigned to three test groups ($n = 8$) and received stereotactic injection of MENPs (100 mg/ml). We tested the washout of MENPs at different time points including 48 hours, 2, and 4 weeks (fig. S4, E and F). At the end of each time point, mice underwent transcardial perfusion, and brains were removed and used for IHC and H&E analysis. To evaluate c-Fos protein expression, two hours before perfusion, half of the mice in each group underwent magnetic stimulation for 180 s. As a control group, the other half of the mice were placed in the coil with no current running through the coil, exposing them only to the DC magnetic field of the permanent magnets. Sections belonging to three mice were excluded for IHC analysis of whole-brain rostrocaudal sections, as tissues were ruptured or damaged during tissue processing. In previous work, IHC quantification with a minimum of five subjects per group has been sufficient for valid analysis (48, 49).

Phase III: Behavioral testing

To evaluate the effect of MENP-induced neuronal modulation on brain tissue, two groups of animals were tested, and behavioral responses were evaluated. Mice were randomly assigned into two groups and received stereotactic injection of either MENPs ($n = 9$) or MSNPs ($n = 8$; 100 mg/ml). Following the recovery period of 1-week postsurgery, animals were stimulated in the magnetic field, and behavioral testing was conducted. Specifically, animals were stimulated with either an AC and DC magnetic field (in the in vivo coil system with the coil on) or with only a DC magnetic field (in the in vivo coil system with the coil off). Measured behavioral parameters were compared between the same mice following stimulation with an AC and DC magnetic field versus stimulation with only a DC magnetic field (fig. S4G).

Behavioral testing
CatWalk test

An automated gait analysis system CatWalk XT (Noldus 7.1, Wageningen, The Netherlands) was to evaluate motor behavior. The CatWalk consists of an enclosed walkway with a glass plate and a speed video recording camera (Fig. 3I). Gait performance was assessed and recorded using the CatWalk analysis software. The glass plate was cleaned and dried before testing each subject to minimize the transmission of olfactory cues and prevent animals from

stopping to smell or explore something during a run. In general, one successful test recording consisted of an average of five uninterrupted runs having a comparable running speed with a maximum variation of 30%. The experimenter and data analyst were blind to animal identity during the behavioral testing and data analysis. The following 20 static and dynamic parameters assessing individual paw functioning and gait patterns were analyzed: stance, mean intensity, print area, print length, print width, swing mean, swing speed, stride length, maximum intensity at maximum contact, maximum intensity, minimum intensity, step cycle, duty cycle, regularity index, base of support of the forelimbs, base of support of the hindlimbs, three limb support, speed, and cadence.

Rotarod test
An accelerating rotarod with a grooved rotating beam (3 cm) raised 16 cm above a platform (model 47650, Ugo Basile Biological Research Apparatus, Italy) was used to measure coordination. The latency to fall off the rotating rod was recorded. Data were expressed as the mean value from three trials. Mice were subjected to four 300-s trials per day for three consecutive days (days 1 to 3) with an intertrial interval of ~15 min. Mice were forced to run on a rotating drum with speeds starting at 4 rpm and accelerating to 40 rpm within 300 s. Mice remaining on the beam during the full 300 s of the task were taken from the rotarod and given the maximum score. The experimenter and data analyst were blind to animal identity during the behavioral testing and data analysis.

Animal sacrifice protocol for IHC analysis of brain tissue
Mice were deeply anaesthetized with pentobarbital and transcardially perfused with tyrode buffer, followed by ice-cold 4% paraformaldehyde fixative in 0.1 M phosphate buffer. The brains were extracted from the crania and postfixed in 4% paraformaldehyde overnight and then submerged in sucrose for cryoprotection (24 hours in 20% sucrose at 5°C). Coronal brain sections (20 μm) were cut on a cryostat and stored at −80°C.

Immunohistochemistry
Tissue sections were incubated overnight with polyclonal rabbit antibodies raised against c-Fos protein (1:1000; Santa Cruz Biotechnology Inc.; sc-253), GFAP (1:1000; Dako; Z-033429), or Iba-1(1:1000; Wako; 016-26461). c-Fos IHC used biotinylated donkey anti-rabbit secondary antibody (1:400; Jackson ImmunoResearch Laboratories Inc.; 711065152) and avidin-biotin peroxidase complex (1:800; Elite ABC-kit, Vector Laboratories; PK-6100). The staining was visualized by 3,3′-diaminobenzidine combined with NiCl2 intensification. GFAP and Iba-1 were visualized using immunofluorescence with donkey anti-rabbit Alexa 488 (1:100; Invitrogen; A-21206).

Quantification of c-Fos immunohistochemically labeled cells
Photographs of the stained motor cortex and thalamus sections from three rostrocaudal anatomical levels from bregma (AP: −0.58, −0.94, and −1.22) were taken at 10X magnification. We used Cell P software (Olympus Soft Imaging Solutions, Münster, Germany) from an Olympus DP70 digital camera connected to an Olympus AX 70 microscope (Olympus, Zoeterwoude, The Netherlands). In the images of the area of interest, the number of c-Fos–positive cells was counted using ImageJ software [version 1.52; National Institutes of Health (NIH), Bethesda, USA]. Cells immunopositive for c-Fos were counted manually, and the mean number of cells was corrected for surface area and expressed as cells per square millimeter. A cell was regarded positive when the intensity of the cell staining was significantly higher than the surrounding background. The average value of three sections was used for statistical analysis in each subject. For the subthalamic area (the infusion site), a digital photograph was taken at one anatomical bregma (−2.06), and all c-Fos–positive cells within 1 mm^2 of the injection site were counted.

Quantification of GFAP and Iba-1 immunohistochemically labeled cells
Photographs of the stained motor cortex and thalamus sections from three rostrocaudal anatomical levels from bregma (AP: −1.70, −2.06, and − 2.30) were taken at ×10 magnification. We used Cell P software (Olympus Soft Imaging Solutions, Münster, Germany) from an Olympus DP70 digital camera connected to an Olympus AX 70 microscope (Olympus, Zoeterwoude, The Netherlands). In the images of the area of interest, fluorescent density was measured using ImageJ software (version 1.52; NIH, Bethesda, USA). The average value of three sections was used for statistical analysis in each subject.

Quantification of MENP distribution and c-Fos expression volumes at the injection site
Stereological volume measurement was carried out on the MENP injection site at subthalamic region and surrounding c-Fos expression area. We used a stereological computer microscopy system (Stereo Investigator, Microbrightfield Bioscience, version 10, Williston, VT, USA). Briefly, after delineation of those regions in c-Fos–stained sections on video images displayed on the monitor, the volumes were calculated with Cavalieri's principle (Cavalieri, 1635) (50). The volume of every part was calculated by multiplying the surface with the section thickness and the number of slices per series. Last, all these parts were summed, and the total volume of the MENP injection site and c-Fos expression area were calculated.

Statistical analysis
Unless otherwise indicated, data are presented as individual values with bars showing the means ± SD. The AC magnetic field magnitude and frequency dependence on MENP voltage output was determined using a linear regression, with coefficient of determination presented as R^2. In vitro Ca^{2+} transient activity and in vivo c-Fos expression were analyzed using a one-way analysis of variance (ANOVA) with Tukey's post-test to compare all groups (fig. S4). In vitro analysis of Ca^{2+} signaling with inhibitors was analyzed using a one-way ANOVA with Dunnett's post-test, using drug-untreated cells as the controls. c-Fos protein expression in brain tissue was analyzed using an unpaired t test. Changes in behavioral parameters in the same mice following stimulation with either a DC magnetic field or an AC and DC magnetic field were analyzed using a paired t test. The experimenter and data analyst were blind to animal identity during the behavioral testing, analysis of behavioral data, and quantification of IHC sections. P values of <0.05 were considered statistically significant in all cases.

SUPPLEMENTARY MATERIALS

REFERENCES AND NOTES
1. A. L. Benabid, P. Pollak, A. Louveau, S. Henry, J. de Rougemont, Combined (thalamotomy and stimulation) stereotactic surgery of the VIM thalamic nucleus for bilateral Parkinson disease. *Appl. Neurophysiol.* **50**, 344–346 (1987).

2. F. B. Wagner, J.-B. Mignardot, C. G. Le Goff-Mignardot, R. Demesmaeker, S. Komi, M. Capogrosso, A. Rowald, I. Seáñez, M. Caban, E. Pirondini, M. Vat, L. A. McCracken, R. Heimgartner, I. Fodor, A. Watrin, P. Seguin, E. Paoles, K. Van Den Keybus, G. Eberle, B. Schurch, E. Pralong, F. Becce, J. Prior, N. Buse, R. Buschman, E. Neufeld, N. Kuster, S. Carda, J. von Zitzewitz, V. Delattre, T. Denison, H. Lambert, K. Minassian, J. Bloch, G. Courtine, Targeted neurotechnology restores walking in humans with spinal cord injury. *Nature* **563**, 65–71 (2018).

3. J. Rivnay, H. Wang, L. Fenno, K. Deisseroth, G. G. Malliaras, Next-generation probes, particles, and proteins for neural interfacing. *Sci. Adv.* **3**, e1601649 (2017).

4. E. de Schlichting, G. Coll, J. F. Zaldivar-Jolissaint, J. Coste, A. R. Marques, A. Mulliez, F. Durif, J.-J. Lemaire, Pulse generator battery life in deep brain stimulation: Out with the old... in with the less durable? *Acta Neurochir.* **161**, 2043–2046 (2019).

5. P. Yeon, M. S. Bakir, M. Ghovanloo, Towards a 1.1 mm² free-floating wireless implantable neural recording SoC, in *2018 IEEE Custom Integrated Circuits Conference (CICC)* (IEEE, 2018), pp. 1–4.

6. S. Lee, A. J. Cortese, A. P. Gandhi, E. R. Agger, P. L. McEuen, A. C. Molnar, A 250 μm× 57 μm microscale opto-electronically transduced electrodes (MOTEs) for neural recording. *IEEE Trans. Biomed. Circuits Syst.* **12**, 1256–1266 (2018).

7. S. Lee, A. J. Cortese, P. Trexel, E. R. Agger, Paul L. McEuen, A. C. Molnar, A 330μm×90μm Opto-electronically integrated wireless system-on-chip for recording of neural activities, in *2018 IEEE International Solid-State Circuits Conference-(ISSCC)* (IEEE, 2018), pp. 292–294.

8. Y.-K. Song, D. A. Borton, S. Park, W. R. Patterson, C. W. Bull, F. Laiwalla, J. Mislow, J. D. Simeral, J. P. Donoghue, A. V. Nurmikko, Active microelectronic neurosensor arrays for implantable brain communication interfaces. *IEEE Trans. Neural Syst. Rehabil. Eng.* **17**, 339–345 (2009).

9. D. Seo, R. M. Neely, K. Shen, U. Singhal, E. Alon, J. M. Rabaey, J. M. Carmena, M. M. Maharbiz, Wireless recording in the peripheral nervous system with ultrasonic neural dust. *Neuron* **91**, 529–539 (2016).

10. M. M. Ghanbari, D. K. Piech, K. Shen, S. Faraji Alamouti, C. Yalcin, B. C. Johnson, J. M. Carmena, M. M. Maharbiz, R. Muller, A Sub-mm³ ultrasonic free-floating implant for multi-mote neural recording. *IEEE J. Solid State Circuits* **54**, 3017–3030 (2019).

11. D. Seo, J. M. Carmena, J. M. Rabaey, M. M. Maharbiz, E. Alon, Model validation of untethered, ultrasonic neural dust motes for cortical recording. *J. Neurosci. Methods* **244**, 114–122 (2015).

12. B. C. Johnson, K. Shen, D. Piech, M Meraj Ghanbari, K. Y. Li, R. Neely, J. M. Carmena, M. M. Maharbiz, R. Muller, StimDust: A 6.5mm³, wireless ultrasonic peripheral nerve stimulator with 82% peak chip efficiency, in *2018 IEEE Custom Integrated Circuits Conference (CICC)* (IEEE, 2018), pp. 1–4.

13. D. K. Piech, B. C. Johnson, K. Shen, M. M. Ghanbari, K. Y. Li, R. M. Neely, J. E. Kay, J. M. Carmena, M. M. Maharbiz, R. Muller, A wireless millimetre-scale implantable neural stimulator with ultrasonically powered bidirectional communication. *Nat. Biomed. Eng.* **4**, 207–222 (2020).

14. A. Marino, S. Arai, Y. Hou, E. Sinibaldi, M. Pellegrino, Y.-T. Chang, B. Mazzolai, V. Mattoli, M. Suzuki, G. Ciofani, Piezoelectric nanoparticle-assisted wireless neuronal stimulation. *ACS Nano* **9**, 7678–7689 (2015).

15. R. Chen, G. Romero, M. G. Christiansen, A. Mohr, P. Anikeeva, Wireless magnetothermal deep brain stimulation. *Science* **347**, 1477–1480 (2015).

16. K. L. Montgomery, A. J. Yeh, J. S. Ho, V. Tsao, S. M. Iyer, L. Grosenick, E. A. Ferenczi, Y. Tanabe, K. Deisseroth, S. L. Delp, A. S. Y. Poon, Wirelessly powered, fully internal optogenetics for brain, spinal and peripheral circuits in mice. *Nat. Methods* **12**, 969–974 (2015).

17. M. J. Weber, A. Bhat, T. C. Chang, J. Charthad, A. Arbabian, A miniaturized ultrasonically powered programmable optogenetic implant stimulator system, in *2016 IEEE Topical Conference on Biomedical Wireless Technologies, Networks, and Sensing Systems (BioWireleSS)* (IEEE, 2016), pp. 12–14.

18. A. Singer, S. Dutta, E. Lewis, Z. Chen, J. C. Chen, N. Verma, B. Avants, A. K. Feldman, J. O'Malley, M. Beierlein, C. Kemere, J. T. Robinson, Magnetoelectric materials for miniature, wireless neural stimulation at therapeutic frequencies. *Neuron* **107**, 631–643.e5 (2020).

19. J. Lee, E. Mok, J. Huang, L. Cui, A.-H. Lee, V. Leung, P. Mercier, S. Shellhammer, L. Larson, P. Asbeck, R. Rao, Y.-K. Song, A. Nurmikko, F. Laiwalla, An implantable wireless network of distributed microscale sensors for neural applications, in *2019 9th International IEEE/EMBS Conference on Neural Engineering (NER)* (IEEE, 2019), pp. 871–874.

20. IEEE Standard for Safety Levels with Respect to Human Exposure to Electric, Magnetic, and Electromagnetic Fields, 0 Hz to 300 GHz, in *IEEE Std C95.1–2019 (Revision of IEEE Std C95.1–2005/ Incorporates IEEE Std C95.1–2019/Cor 1–2019)* (2019), pp. 1–312.

21. C. Gabriel, S. Gabriel, E. Corthout, The dielectric properties of biological tissues: I. Literature survey. *Phys. Med. Biol.* **41**, 2231–2249 (1996).

22. P. S. Tofts, The distribution of induced currents in magnetic stimulation of the nervous system. *Phys. Med. Biol.* **35**, 1119–1128 (1990).

23. W. Klomjai, R. Katz, A. Lackmy-Vallée, Basic principles of transcranial magnetic stimulation (TMS) and repetitive TMS (rTMS). *Ann. Phys. Rehabil. Med.* **58**, 208–213 (2015).

24. Z.-D. Deng, S. H. Lisanby, A. V. Peterchev, Electric field depth-focality tradeoff in transcranial magnetic stimulation: Simulation comparison of 50 coil designs. *Brain Stimul.* **6**, 1–13 (2013).

25. Y. Roth, A. Amir, Y. Levkovitz, A. Zangen, Three-dimensional distribution of the electric field induced in the brain by transcranial magnetic stimulation using figure-8 and deep H-coils. *J. Clin. Neurophysiol.* **24**, 31–38 (2007).

26. R. Guduru, P. Liang, J. Hong, A. Rodzinski, A. Hadjikhani, J. Horstmyer, E. Levister, S. Khizroev, Magnetoelectric 'spin' on stimulating the brain. *Nanomedicine* **10**, 2051–2061 (2015).

27. V. Corral-Flores, D. Bueno-Baqués, R. F. Ziolo, Synthesis and characterization of novel CoFe₂O₄-BaTiO₃ multiferroic core-shell-type nanostructures. *Acta Mater.* **58**, 764–769 (2010).

28. V. Corral-Flores, D. Bueno-Baques, D. Carrillo-Flores, J. A. Matutes-Aquino, Enhanced magnetoelectric effect in core-shell particulate composites. *J. Appl. Phys.* **99**, 08J503 (2006).

29. G. V. Duong, R. Groessinger, M. Schoenhart, D. Bueno-Basques, The lock-in technique for studying magnetoelectric effect. *J. Magn. Magn. Mater.* **316**, 390–393 (2007).

30. G. V. Duong, R. Groessinger, R. S. Turtelli, Magnetoelectric properties of CoFe₂O₄-BaTiO₃ core-shell structure composite. *IEEE Trans. Magn.* **42**, 3611–3613 (2006).

31. M. M. Vopson, Y. K. Fetisov, G. Caruntu, G. Srinivasan, Measurement techniques of the magneto-electric coupling in multiferroics. *Materials* **10**, 963 (2017).

32. E. B. Montgomery Jr., J. T. Gale, Mechanisms of action of deep brain stimulation(DBS). *Neurosci. Biobehav. Rev.* **32**, 388–407 (2008).

33. J. I. Morgan, T. Curran, Role of ion flux in the control of c-*fos* expression. *Nature* **322**, 552–555 (1986).

34. M. Bichurin, V. M. Petrov, R. V. Petrov, Y. V. Kiliba, F. I. Bukashev, A. Y. Smirnov, D. N. Eliseev, Magnetoelectric sensor of magnetic field. *Ferroelectrics* **280**, 199–202 (2002).

35. D. J. Lee, C. S. Lozano, R. F. Dallapiazza, A. M. Lozano, Current and future directions of deep brain stimulation for neurological and psychiatric disorders. *J. Neurosurg.* **131**, 333–342 (2019).

36. H. Bergman, T. Wichmann, M. R. DeLong, Reversal of experimental parkinsonism by lesions of the subthalamic nucleus. *Science* **249**, 1436–1438 (1990).

37. T. Wichmann, M. R. DeLong, Pathophysiology of parkinsonian motor abnormalities. *Adv. Neurol.* **60**, 53–61 (1993).

38. A. Nambu, H. Tokuno, M. Takada, Functional significance of the cortico-subthalamo-pallidal 'hyperdirect' pathway. *Neurosci. Res.* **43**, 111–117 (2002).

39. G. E. Alexander, M. D. Crutcher, M. R. DeLong, Basal ganglia-thalamocortical circuits: Parallel substrates for motor, oculomotor, "prefrontal" and "limbic" functions. *Prog. Brain Res.* **85**, 119–146 (1990).

40. G. J. Kirouac, Placing the paraventricular nucleus of the thalamus within the brain circuits that control behavior. *Neurosci. Biobehav. Rev.* **56**, 315–329 (2015).

41. C. Bellardita, O. Kiehn, Phenotypic characterization of speed-associated gait changes in mice reveals modular organization of locomotor networks. *Curr. Biol.* **25**, 1426–1436 (2015).

42. V. Caggiano, R. Leiras, H. Goñi-Erro, D. Masini, C. Bellardita, J. Bouvier, V. Caldeira, G. Fisone, O. Kiehn, Midbrain circuits that set locomotor speed and gait selection. *Nature* **553**, 455–460 (2018).

43. F. Agnesi, A. T. Connolly, K. B. Baker, J. L. Vitek, M. D. Johnson, Deep brain stimulation imposes complex informational lesions. *PLOS ONE* **8**, e74462 (2013).

44. M. Jakobs, A. Fomenko, A. M. Lozano, K. L. Kiening, Cellular, molecular, and clinical mechanisms of action of deep brain stimulation–a systematic review on established indications and outlook on future developments. *EMBO Mol. Med.* **11**, e9575 (2019).

45. J. B. Ranck Jr., Which elements are excited in electrical stimulation of mammalian central nervous system: A review. *Brain Res.* **98**, 417–440 (1975).

46. F. Rattay, The basic mechanism for the electrical stimulation of the nervous system. *Neuroscience* **89**, 335–346 (1999).

47. H. Davson, *Physiology of the Cerebrospinal Fluid* (Churchill, London, 1967).

48. A. Jahanshahi, R. Vlamings, A. H. Kaya, L. W. Lim, M. L. F. Janssen, S. Tan, V. Visser-Vandewalle, H. W. M. Steinbusch, Y. Temel, Hyperdopaminergic status in experimental Huntington disease. *J. Neuropathol. Exp. Neurol.* **69**, 910–917 (2010).

49. A. Jahanshahi, R. Vlamings, W. M. C. van Roon-Mom, R. L. M. Faull, H. J. Waldvogel, M. L. F. Janssen, Y. Yakkioui, D. H. Zeef, E. Kocabicak, H. W. M. Steinbusch, Y. Temel, Changes in brainstem serotonergic and dopaminergic cell populations in experimental and clinical Huntington's disease. *Neuroscience* **238**, 71–81 (2013).

50. C. Schmitz, P. R. Hof, Recommendations for straightforward and rigorous methods of counting neurons based on a computer simulation approach. *J. Chem. Neuroanat.* **20**, 93–114 (2000).

Citation: K. L. Kozielski, A. Jahanshahi, H. B. Gilbert, Y. Yu, Ö. Erin, D. Francisco, F. Alosaimi, Y. Temel, M. Sitti, Nonresonant powering of injectable nanoelectrodes enables wireless deep brain stimulation in freely moving mice. *Sci. Adv.* **7**, eabc4189 (2021).